PERGAMON

International Journal of Heat and Mass Transfer 44 (2001) 2681–2697

International Journal of HEAT and MASS TRANSFER

www.elsevier.com/locate/ijhmt

Numerical and laboratory experiments of sidewall heating thermohaline convection

C. Sabbah [a], R. Pasquetti [a,*], R. Peyret [a], V. Levitsky [b], Y.D. Chashechkin [b]

[a] *Laboratory J.A. Dieudonné, UNSA, UMR CNRS 6621, Nice, France*
[b] *Institute for Problems in Mechanics, Moscow, Russian Federation*

Received 30 May 2000; received in revised form 8 September 2000

Abstract

The spectral calculations of the flow which develops near a heated vertical wall in a fluid stably stratified by a salinity gradient are carried out. The case of weak stratification and heating due to a constant heat flux is considered. The numerical results are compared to the experimental ones. Both on qualitative and quantitative arguments, a satisfactory agreement is obtained. The cell formation process is discussed by focusing on the occurrence of counter-rotative cells and on the instability phenomenon of the simultaneous creation of cells. The high sensitivity of such phenomena to slight disturbances at the initial time is pointed out. © 2001 Published by Elsevier Science Ltd. All rights reserved.

1. Introduction

Thermohaline experiments were mainly stimulated by the discovery of layered structures in ocean or in atmosphere, where thick homogeneous layers are separated by thin high gradient interfaces (see e.g. [1]). It is now recognized that one mechanism which can lead to the formation of such sharp interfaces is the double diffusive convection, i.e., a convective flow driven by buoyancy forces in a two-component medium with different diffusivities. This kind of convection manifests itself by the splitting of the initial smooth density profile into a system of layers separated by high density gradients. The reviews of early investigations are presented in [2,3]. As observed in many experiments, convecting layers form in a continuously stratified salt solution under bottom heating [4], above horizontal cylinders [5] or point heat sources [6,7], under side heating in slots [8–11] or, as considered in this paper, in tanks [12–17], as soon as the overheating exceeds some critical value. The distinction between slots and tanks refers to their width with respect to the "potential rise" of an overheated fluid particle. Notice also that double diffusive convection studies have applications not only in the domain of oceanography but also in other fields like safety in gas-storage (overrolling problem in gas reservoirs) [18].

Thermohaline convection constitutes a challenge to the numerical methods: due to high value of the Lewis number, $Le = \kappa_T/\kappa_S \approx 100$, where κ_T and κ_S are the thermal and salt diffusivities, respectively, the salt is essentially transported, so that very sharp interfaces form between convective cells of nearly uniform salt concentration. Of course, coarse grids had to be used in earlier calculations which considered the case of thermohaline convection in slots [19–21]. Later, thanks to the increasing capabilities of computers, it has become possible to conduct calculations in tanks and for higher values of the "Rayleigh number" [22,23]. Usually the temperature is prescribed at the heating wall but in some studies it is the heat flux density which is imposed [23,24]. Also, at the initial time the fluid is generally assumed to be isothermal, but some papers investigate the situation where the fluid is initially both stratified in temperature and salinity [24,25]. More often, low-order methods like finite difference [19,25,26], finite volume [22–24] or finite element [20] methods are used, but in [21,27] spectral calculations are carried out. However, in

* Corresponding author.

0017-9310/01/$ - see front matter
PII: S0017-9310(00)00307-0

[23] an adaptative two-block composite grid strategy is used in order to accumulate grid points near the heating wall, on the contrary of what is done in [25,26] where equidistant grids are used.

For such calculations, spectral methods are well suited because their high accuracy allows a fine description of the physical phenomena. Moreover, simple shape of the computational domain makes the Chebyshev method very attractive and the use of a multi-domain technique leads to efficient algorithms well adapted to parallel computations. Thus, the spectral multi-domain method described in [28,29] is used here to compute the convective flow observed in the laboratory experiments that we have carried out. However, performing this simulation was a real challenge, due to the size of cells compared to the height of the heating wall, and a rather important number of grid-points ($\approx 6 \times 10^5$) has been used to perform a reliable 2D numerical calculation. However, as mentioned in [30], 3D investigations could be desirable, but the satisfactory agreement obtained here between our experimental and numerical investigations gives a justification for the 2D approximation.

In this paper, we are essentially interested in the cell formation process. Thus, counter-rotating cells are difficult to observe experimentally, whereas they are predicted by the linear stability analyses [9,31] and easier to obtain numerically. Moreover, after the earlier formation of a few cells at the extremities of the heater, the cells can form *simultaneously* along the heated wall or *successively*, as already discussed in [8]. Concerning this cell creation process, the numerical approaches may be in disagreement: the numerical results of [21,23,27] only show the *successive* creation of convective cells, first at the lower wall and later at the upper one, whereas in the calculations of [22,25,26] the *simultaneous* creation seems to be obtained. On the experimental side, after the formation of the first cells the simultaneous creation is generally observed (see e.g. [8,12,13]). For the first time, to our knowledge, the present calculations show that the occurrence of the successive or simultaneous creation process is strongly linked to the amplitude of initial disturbances, at least when high-order methods are involved. In the same way, it is clearly pointed out that counter-rotating cells are much more intense when no disturbances are used at the initial time, so that some disagreements between the experimental observations and theoretical or numerical investigations may be better understood.

The paper is organized as follows: Section 2 is devoted to a brief description of the experimental setup, to its modelling and to the spectral-Chebyshev multi-domain method used to solve the governing equations. In Section 3, the results of the numerical simulation are presented and comparisons with the experimental results are provided. In Section 4, we point out the influence of initial disturbances on the cell formation process and, finally, conclude in Section 5.

2. Experimental setup, modelling and numerical method

2.1. Experimental setup

Here we only recall the basic elements required for a good understanding of the paper, since more details on the experimental setup and techniques can be found elsewhere, e.g., in [32]. The tank height, length and horizontal width are, respectively, 50, 50 and 15 cm. The bottom and vertical walls are isolated and the free upper surface is covered by a plastic sheet. At the centre of the tank two different heaters can be used: a water-heater or an electric heater. Using the water-heater (flat heat exchanger) approximately permits to impose the temperature, whereas with the electric heater one can control the heat flux density φ.

A two-tank system is used to fill the tank with a linearly stratified fluid, i.e., such that the salinity gradient is constant and downwards. Its value is measured thanks to an electric conductivity sensor: the electric conductivity being connected to salinity, a slight disturbance of the fluid induces oscillations of the conductivity at the buoyancy period T_b. Then the Brunt–Väisälä angular frequency N and the characteristic length Λ of the stratification are obtained, respectively, from the relations $NT_b = 2\pi$ and $N^2\Lambda = g$. The salinity difference, δS, between the top and bottom of the tank can be determined from the relation $\beta\delta S = H/\Lambda$, where β is the salinity expansion coefficient and H is the height of the tank. Let us recall that N is in fact only constant for an exponentially stratified fluid, since $N^2 = -(g/\rho)(\partial\rho/\partial y)$. However, assuming a constant value of N is valid as soon as $H \ll \Lambda$.

Temperature probes are located inside the tank: especially, the environment temperature, mean temperature of the electric heater and temperatures of the vertical walls opposite to the heater are measured. A Schlieren system is used to visualize the flow, by providing an image connected with $\partial_x n$, the partial derivative of the fluid refractive index n with respect to the horizontal axis x, itself connected with $\partial_x \rho$, due to the dependence of ρ on n.

Comparisons between the numerical and experimental results will be done for the experiments conducted with the electric heater, for which the boundary condition is well controlled: the heat flux density φ may be assumed to be uniform on the heater and the global flux results from voltage and electric current measurements. The height of the electric heater is equal to 30 cm, leaving a free space of 10 cm at the top and at the bottom of the tank.

From the experiment one can deduce several characteristic parameters of the flow, like the mean height and width of the cells, as well as derived quantities such as the ratio K_a of the mean height to the height $h_a = \alpha\delta T\Lambda$ to which an overheated fluid particle would rise in the initial density gradient [12].

2.2. Modelling

Computational domain. For obvious symmetry reasons, only the part of the tank on the right-hand side of the heater is considered, as shown in Fig. 1. Moreover, to decrease the computation cost and knowing that far from the heater the fluid is nearly at rest, the half-width is taken to be smaller, $L = 12$ cm rather than 25 cm. On the contrary, the height has been kept equal to $H = 50$ cm, since we are not only interested in local phenomena but also in the global phenomenon of the simultaneous creation of convective cells.

Initial conditions. At the initial time the fluid is at rest. The temperature is homogeneous. The salinity gradient is constant and downwards.

Boundary conditions. Neumann boundary conditions are used for temperature. The electric heater is modelled by a time-independent and uniform heat flux density, which vanishes regularly at the heater extremities. In agreement with the heater technology, 2 mm on each side are used to this end. Elsewhere, the heat flux density is assumed as null: (i) for symmetry reasons, above and below the heater, (ii) by assuming that the isolated walls of the tank are perfectly adiabatic and also (iii) by neglecting the thermal losses at the upper fluid surface. Such assumptions are realistic, when knowing that the overheating on the heater is about 1 K. Homogeneous Neumann (no-penetration) conditions are used for salinity and no-slip conditions are used for velocity.

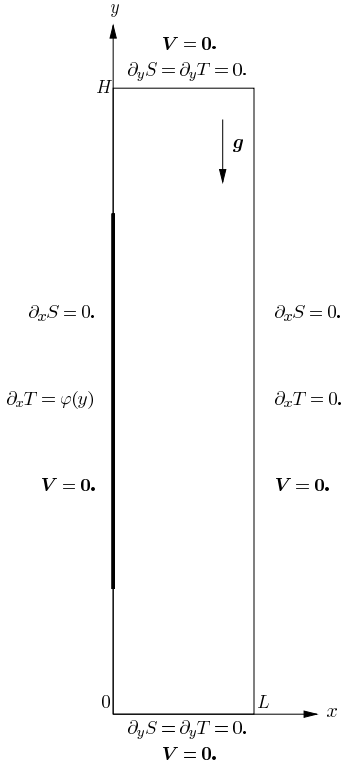

Fig. 1. Geometrical configuration and boundary conditions.

Governing equations. The fluid motion and the heat and salinity transfers are modelled within the Boussinesq approximation. Thus, (i) the fluid flow is governed by the incompressible Navier–Stokes equations coupled to transport-diffusion equations for temperature and salinity, (ii) the density variations are only considered in the buoyancy term and assumed as linearly dependent on the variations of temperature and salinity to their mean values at the initial time.

The partial differential equations can then be written in dimensionless form

$$\frac{1}{Pr}D_t\boldsymbol{V} = -\nabla p + Ra_\varphi(T - R_\rho S)\boldsymbol{e}_y + \Delta\boldsymbol{V}, \tag{1}$$

$$\nabla\cdot\boldsymbol{V} = 0, \tag{2}$$

$$D_tT = \Delta T, \tag{3}$$

$$D_tS = \frac{1}{Le}\Delta S \tag{4}$$

with $\boldsymbol{e}_y$ for the unit vertical vector, t for the time, $\boldsymbol{V}$ for the velocity, p for the deviation of pressure from the hydrostatic one, T and S, respectively, for the deviations of temperature and salinity concentration from their mean initial values and D_t for the material derivative. These quantities have been made dimensionless by using the following reference values: L, L^2/κ_T, κ_T/L, $\rho\nu\kappa_T/L^2$, $L\varphi/\lambda$ and δS, where ρ, λ and ν are the density, the conductivity and the kinematic viscosity, respectively. The Prandtl ($Pr = \nu/\kappa_T$) and Lewis ($Le = \kappa_T/\kappa_S$) numbers are the characteristic parameters of the fluid, whereas the Rayleigh number Ra_φ and the buoyancy ratio R_ρ are characteristics of the flow. For the present problem they are defined by

$$Ra_\varphi = \frac{\alpha\varphi g L^4}{\kappa_T\nu\lambda}, \quad R_\rho = \frac{\beta\delta S\lambda}{\alpha\varphi L} = \frac{H\lambda}{\Lambda\alpha\varphi L} \tag{5}$$

Note that the choice of L as characteristic length is convenient for modelling, but, from a physical point of view, really justified for slot type domains only. However, it is always possible to use a convenient reference length for the calculations and then to discuss the numerical results by using other reference lengths. This is

what is done in our analysis of the numerical and experimental results.

2.3. Numerical method

Discretization in time. The time derivatives are discretized by using a second-order finite difference backward Euler approximation. The linear terms are treated implicitly and the convective terms explicitly, by using a second-order Adams–Bashforth extrapolation, except for the salinity which is treated implicitly. For salinity equation, large value of the Lewis number would lead to very small time-steps if the term $\boldsymbol{V}\cdot\nabla S$ was treated in an explicit way. Considering this term implicitly strongly reduces the constraint on the time-step but, of course, necessitates the use of an iterative procedure.

• *Discretization in space*. Along the vertical direction a domain decomposition technique is combined to a parallel calculation, each sub-domain being associated to a processor. At the interfaces between the subdomains, the essential and natural transmission conditions are imposed. In each sub-domain, a pseudo-spectral method is used to solve at each time-cycle and successively (i) a Helmholtz equation for temperature, (ii) a steady advection–diffusion-type equation for salinity and (iii) a generalized Stokes problem for velocity and pressure fields. The partial differential equations are approximated with the Chebyshev collocation method using a strong formulation. The general Stokes problem is solved with the same vector space for both the velocity components and pressure.

Finally, with $\mathrm{P}_{I,J}$ the space of the polynomials of maximum degree I in x (horizontal axis) and J in y (vertical axis), $\overline{\Omega}^k_{I,J}$ the set of the grid-points of the sub-domain $\overline{\Omega}^k$ $(1\leqslant k\leqslant K)$ and $\Omega^k_{I,J}$ the sub-set of the inner points, at each time-cycle one solves the following problem:

For $k=1,\ldots,K$, find $\boldsymbol{V}$ in $\mathrm{P}^2_{I,J}(\overline{\Omega}^k)$ and p, T, S in $\mathrm{P}_{I,J}(\overline{\Omega}^k)$ such as:

$$\Delta T-\sigma_{\mathrm{T}}T=f_{\mathrm{T}}\quad\text{in }\Omega^k_{I,J}, \tag{6}$$

$$\Delta S-Le\boldsymbol{V}^*\cdot\nabla S-\sigma_{\mathrm{S}}S=f_{\mathrm{S}}\quad\text{in }\Omega^k_{I,J}, \tag{7}$$

$$\Delta\boldsymbol{V}-\sigma_V\boldsymbol{V}-\nabla p=\boldsymbol{f}_V(T,S)\quad\text{in }\Omega^k_{I,J}, \tag{8}$$

$$\nabla\cdot\boldsymbol{V}=0\quad\text{in }\overline{\Omega}^k_{I,J} \tag{9}$$

$$+\text{ boundary conditions} \tag{10}$$

with the following continuity constraints: for $k=1,\ldots,K-1$

$$[\![\boldsymbol{V}]\!]_k=[\![T]\!]_k=[\![S]\!]_k=0, \tag{11}$$

$$[\![\partial_y V_x]\!]_k=[\![\partial_y T]\!]_k=[\![\partial_y S]\!]_k=[\![p]\!]_k=0, \tag{12}$$

where $[\![\cdot]\!]_k$ is the jump at the interface $I_k=\overline{\Omega}^k\cap\overline{\Omega}^{k+1}$.

Expressions of the coefficients σ and terms f directly result from the time-discretization. The velocity $\boldsymbol{V}^*$, in the Eq. (7), is calculated from the values of velocity at the two previous time-cycles, using a second-order extrapolation.

The problem (6)–(10) is first solved with homogeneous values of the unknowns at the interfaces, but taking into account the forcing terms and the boundary conditions. Then, the correct interface values are determined by using influence matrices to impose the transmission conditions. These influence matrices, which are computed in preliminary calculations, associate for the corresponding homogeneous problem the interface values to the jumps. Then, the full problem is solved with the correct values of T, S and $\boldsymbol{V}$ at the interfaces. In each sub-domain: (i) equation for the temperature is solved by a direct method, (ii) for the salinity equation one uses the "Preconditioned Conjugate Residual" (see e.g. [33]) iterative procedure, with the Helmholtz operator $\Delta-\sigma_S$ as preconditioner, and (iii) the generalized Stokes problem is solved in a direct way, using a Poisson's equation for pressure. The pressure boundary value is calculated by using again an influence matrix technique, yielding a divergence-free velocity field. Nevertheless, due to the use of the $\mathbb{P}_N-\mathbb{P}_N$-type approximation, the pressure is not unique and is affected by the so-called spurious modes of pressure. Consequently, transmission conditions on pressure, $[\![p]\!]_k=0$, cannot be enforced strongly. The difficulty has been overcome by imposing them weakly, using as trial functions a set of polynomials orthogonal to the pressure space kernel. The details of the algorithm are given in [28].

Finally, we have to mention that to avoid too small values of the dimensionless time-step, which could induce inaccuracies, the reference values for time and velocity are, respectively, divided and multiplied by $(Ra_\varphi)^{0.5}$.

3. Numerical and experimental results

Calculations have been done with the following values of the characteristic dimensionless numbers: $Pr=7$, $Le=100$, $Ra_\varphi=3.46\times10^8$ and $R_\rho=1.66$. For the space discretization we use $K=34$ sub-domains, with $I=250$ and $J=70$ in each sub-domain, i.e., about 6×10^5 grid-points. A coordinate transform is used in x to accumulate mesh points near the heater where the flow is especially complex. In physical units the time-step is $\tau\approx0.2$ s. Two simulations (S1 and S2) have been performed, till the final time $t_{\mathrm{F}}=30$ mn. These simulations differ from the initial condition for temperature: for S2 the initial temperature is randomly disturbed with an amplitude equal to 0.014 K whereas no disturbances are used for S1. As expected, the disturbed calculation S2 yields the

Table 1
Stratification characteristic length (Λ), fluid temperature (T_f), mean heat flux density (φ_m), Prandtl (Pr), Lewis (Le), Rayleigh (Ra_φ) numbers and buoyancy ratio (R_ρ) for the experiments and for the simulations

Exp.	Λ (m)	T_f (°C)	φ_m (W m^{-2})	Pr	Le	Ra_φ	R_ρ
E1	107.8	18	71.9	7.15	99.3	3.23×10^8	1.72
E2	108.6	19	74.2	7.08	100	3.51×10^8	1.57
S1, S2	103.2	20	69.4	7	100	3.46×10^8	1.66

results in a better agreement with the experimental data and so are used in this section. The results obtained for the simulation S1 will be compared to those of S2 in Section 5, in order to study the influence of initial disturbances.

A set of laboratory experiments have been done with a weak background salinity, the upper layer being freshwater (at the lower $S = 5‰$). We focus on two of them (E1 and E2), which yield values of the dimensionless numbers approximately equal to those used in the calculations, as shown in Table 1 where values used for the numerical simulations are also given (T_f stands for the temperature used to estimate the values of the fluid physical parameters and φ_m for the mean heat flux density during the experiments).

The main difficulty in the determination of the different dimensionless numbers comes from the thermal expansion coefficient α, which strongly depends on both the salinity and temperature. Here we have simply considered its values for fresh water, since the salinity is very low. However, it may be observed, in Eq. (5), that α appears only through the product $\alpha\varphi$, so that for the numerical calculations a change in the value of α may be balanced by a change in φ.

The values of α that are used in Table 1 are: α (18°C) $= 1.85 \times 10^{-4}$ K^{-1}, α (19°C) $= 1.96 \times 10^{-4}$ K^{-1} and α (20°C) $= 2.06 \times 10^{-4}$ K^{-1}.

Note that for the sake of simplicity, the same notations are used for the values with or without dimension, the dimension being mentioned in the latter case. To go easily from ones to others, the main reference values are listed in Table 2.

3.1. Numerical results

Figs. 2–5 show the results obtained with the simulation S2. The isolines of the vorticity ω, the stream-function ψ, the temperature T and the salinity S are, respectively, displayed, at the different times $t = \{t_1 = 0.0048,\ t_2 = 0.006,\ t_3 = 0.012,\ t_4 (= t_F) = 0.018\}$ ($t = \{8, 10, 20, 30$ mn$\}$ in physical units). In Fig. 6 the $\partial_x \rho$ fields are given, at the same times. They may be viewed as the pictures provided by the optical Schlieren system. Notice that these figures only visualize the "active part" of the computational domain: elsewhere the fluid is nearly at rest. However, one observes, away from the convective cells and the heat front, horizontal stripes associated with a modulation along the vertical direction. These stripes constitute a system of dissipative gravity waves which propagate into the undisturbed fluid. It is interesting that the calculation has captured this wave-phenomenon which was analyzed earlier, both on its theoretical and experimental aspects [32,34,35]. Fig. 7 gives enlargements of the temperature and salinity fields at the final time t_F, in order to show the complexity of the temperature and salinity fields, with the steep gradients of salinity at the interfaces of the convective cells.

Essentially, the following phenomena have been observed:

- An up-flow forms along the heater, inducing a distortion to the salinity isolines, together with convective cells beginning to form at its extremities, first at the bottom and then at the top. Afterwards new cells appear on contact with the first ones which go on growing. This is a phase of *successive creation* of cells. In the central part and near the heater, the streamlines are vertical.
- At $t \approx t_1$, the *simultaneous creation* of a set of cells occurs. Just before, oscillations of the streamlines are observed as well as the appearance, in the $\partial_x \rho$ field, of horizontal stripes, away from the heater. At time $t \approx t_2$ a pattern of cells can be observed all along the heater.

Table 2
Main reference values for the different variables

Length L	Time $L^2 \kappa_T^{-1}$	Velocity $\kappa_T L^{-1}$	Vorticity $\kappa_T L^{-2}$
0.12 m	$\approx 10^5$ s	1.18×10^{-6} m s^{-1}	0.99×10^{-5} s^{-1}
Stream-function κ_T		Temperature $L\varphi\lambda^{-1}$	Salinity $H\Lambda^{-1}\beta^{-1}$
1.42×10^{-7} m^2 s^{-1}		14.1 K	$\approx 5‰$

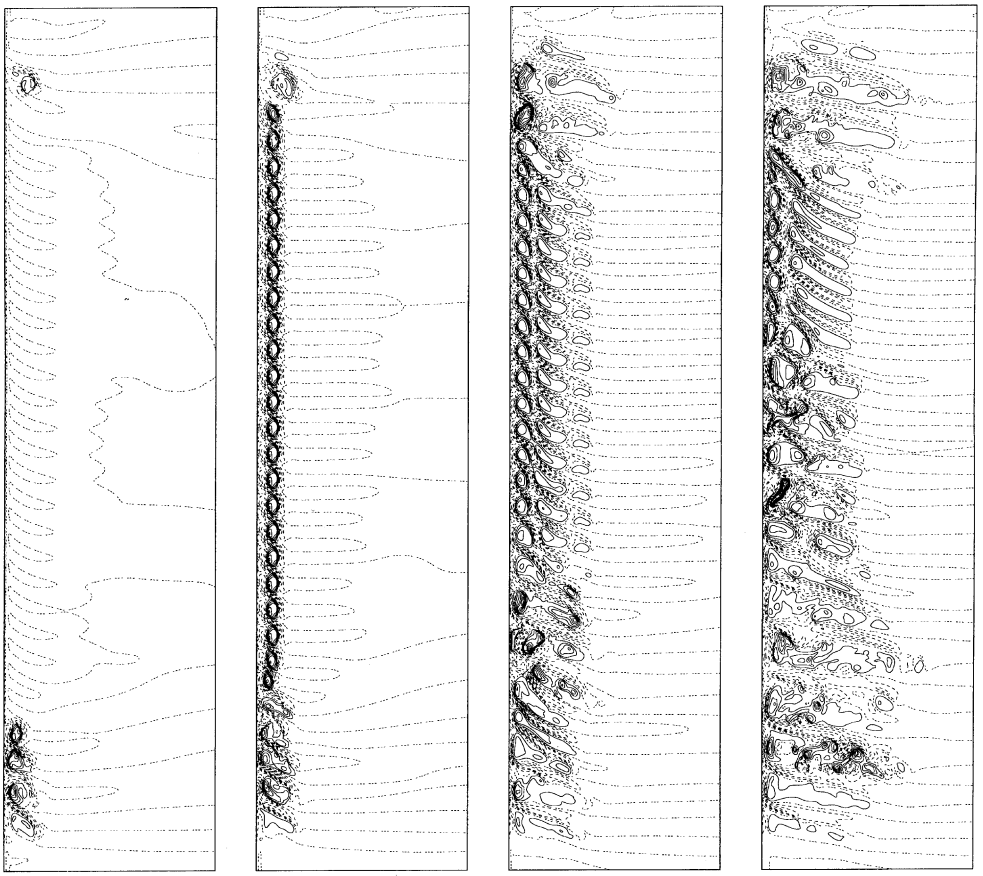

Fig. 2. Vorticity ω at $t = t_i,\ i = 1,\ldots,4$, for $0 \leqslant x \leqslant 0.68$ and $0.75 \leqslant y \leqslant 3.5$ (N.B. full lines are used for negative values).

- Then the cell width is increasing, by means of a doubling process: each cell develops into a set of two small internal cells and, later, into a set of three internal cells. This growing process is especially visible on the $\partial_x \rho$ fields. In the meantime, the stripes stretch out, but keep the vertical periodicity corresponding to the height of the convective cells at their creation.
- The mean height of the cells is increasing by way of merging. This process first begins at the extremities of the heater and then propagates towards its central part.
- Within each cell and internal cells, the salt concentration tends to become homogeneous. This induces rich fine structures limited by stiff salinity gradients at the different outer and inner interfaces.

3.2. Comparisons of the numerical and experimental data

Beyond the good agreement of the experimental and numerical flow pattern evolutions, especially with first the formation of convective cells at the extremities of the heater and then with the simultaneous creation of a set of convective cells, quantitative comparisons have also been carried out. Thus, we have compared the evolution of the mean temperature rise δT_{m} of the heater as well as the mean height h_{m} and width l_{m} of the cells for the experiments E1 and E2 and for the simulation S2. For both the experiments and the simulation, these geometrical quantities have been obtained by focusing on the central part of the heater, i.e., along about 15 cm. The values of h_{m} are easily obtained, e.g., from the $\partial_x \rho$ field. The determination of l_{m} is less straightforward (see e.g., the different fields at $t = t_1$). We have used the temperature field to get an estimate of the "heat front location". Moreover, we have also compared derived quantities, like:

- the Rayleigh number based on the measured (or computed) overheating and on the rising height h_{a} of an overheated fluid particle to reach its new neutral buoyancy level [12]

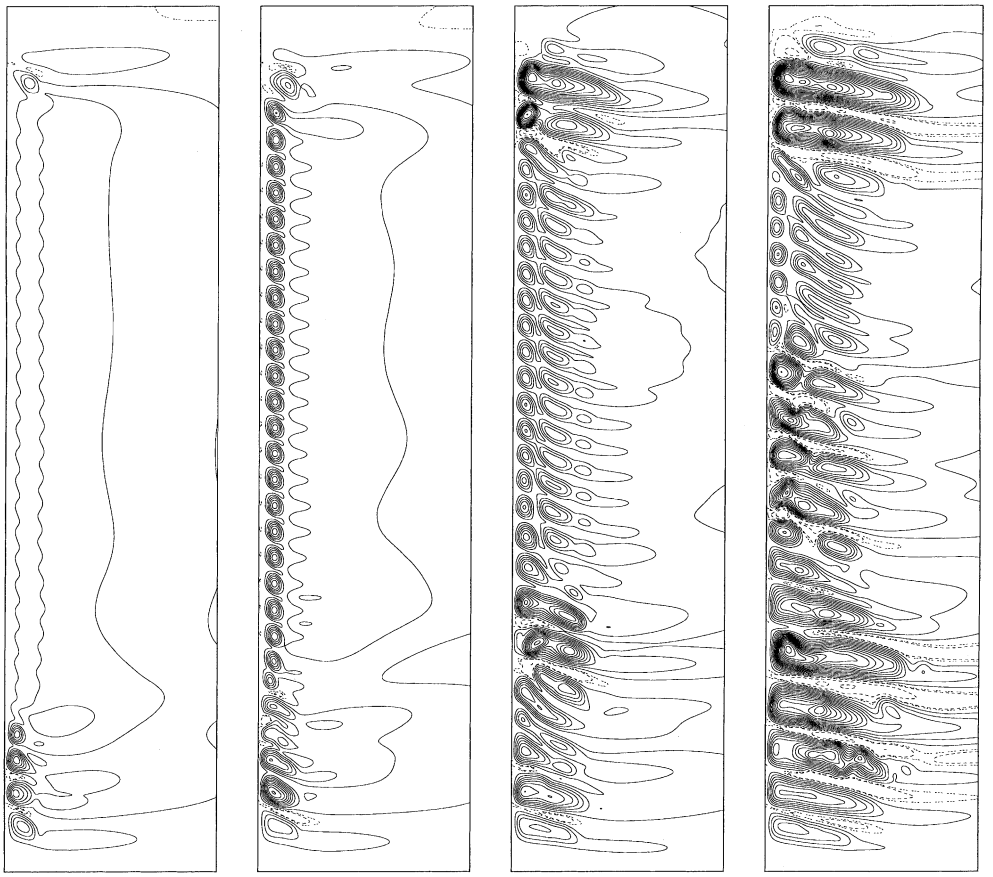

Fig. 3. Stream-function ψ at $t = t_i,\ i = 1, \ldots, 4$, for $0 \leqslant x \leqslant 0.68$ and $0.75 \leqslant y \leqslant 3.5$ (N.B. full lines are used for negative values).

$$Ra = \frac{\alpha g \delta T h_a^3}{\nu \kappa_T}, \quad h_a = \alpha \delta T \Lambda,$$

- the factor K_a equal to the ratio of the mean height of the cells to the potential rising height h_a: $K_a = h_m/h_a$.

Tables 3–5 give the results obtained for the experiments E1 and E2 and for the simulation S2. At different times, one can compare δT_m, h_m, l_m, K_a and Ra. The numerical results appear to be in good agreement with the experiment E1, although the mean height of the cells is a little smaller for the calculation than for the experiments, with a direct influence on the ratio K_a. They compare worse with the experiment E2, for which the mean heat flux density is higher, especially when focusing on the Rayleigh number Ra. This mainly results from the high sensitivity of this number to the product $\alpha\delta T$, since $Ra \propto (\alpha\delta T)^4$. Thus a 20% discrepancy on δT induces a 100% difference on Ra. Moreover, it can be observed that the experiments themselves do not compare very well. This may result from a poor knowledge of the real value of the thermal expansion coefficient α. One has also to mention that the experimental heat flux density is only nearly a constant, with some peaks at about 80 W m^{-2}.

One observes at the end of the calculation that the Rayleigh number Ra reaches rather high values, especially far beyond the critical value associated with the simultaneous creation of cells, 15000 ± 2500 in [12], 4500 ± 1000 in [13] or 18000 ± 5000 in [16]. Note that the discrepancy between these values may also result from a poor knowledge of α.

Using again as reference length the potential rise h_a one can also define a Nusselt number

$$Nu = \frac{\varphi h_a}{\lambda \delta T} = \frac{\varphi \alpha \Lambda}{\lambda}.$$

This time-independent number is nothing but the dimensionless number π_3 introduced in [36] for the characterization of sidewall heating with constant heat flux density. Let us remark here that choosing H rather than L as characteristic length would result in $R_\rho = Nu^{-1}$ in Eq. (1).

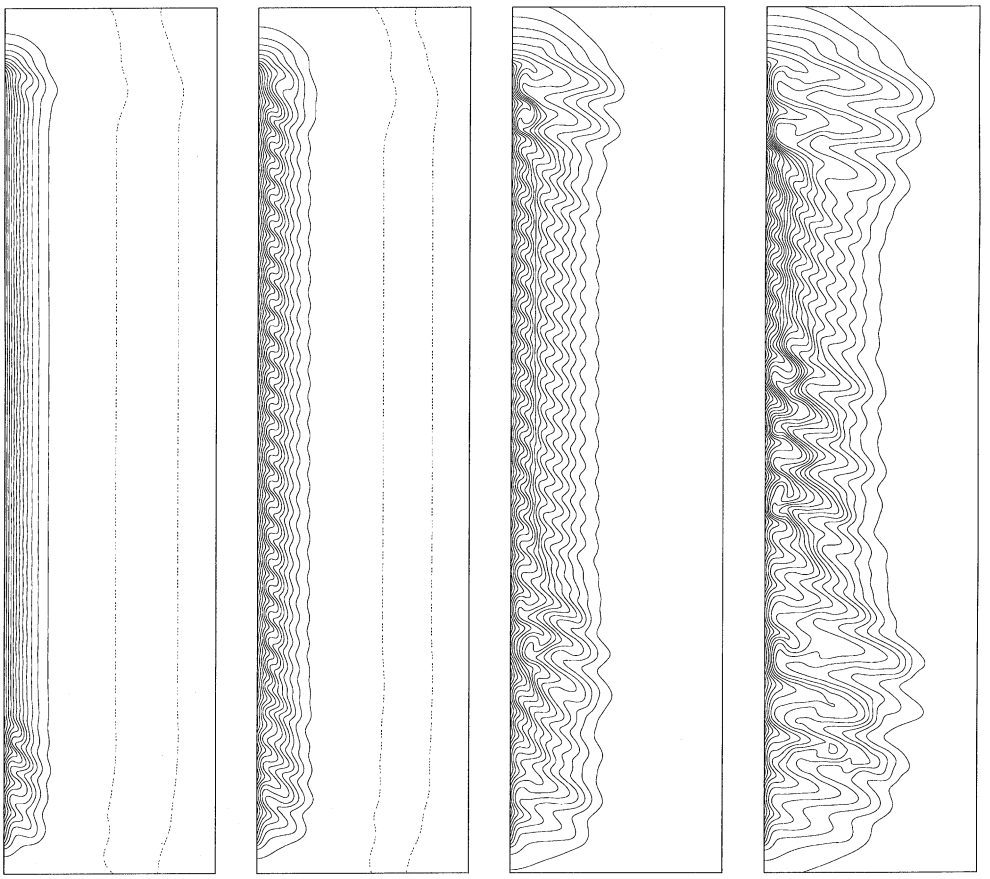

Fig. 4. Temperature T at $t = t_i,\ i = 1, \ldots, 4$, for $0 \leqslant x \leqslant 0.68$ and $0.75 \leqslant y \leqslant 3.5$.

For this Nusselt number, using for the experiments the mean value φ_m of the heat flux density, one obtains: $Nu(\mathrm{E1}) \approx 2.43$, $Nu(\mathrm{E2}) \approx 2.68$ and $Nu(\mathrm{S2}) \approx 2.50$. One observes that despite discrepancies between the input parameters, the $Nu(\mathrm{S2})$ value is well adapted. Again we have to mention the importance of the parameter α in the present problem: Ra_φ, R_ρ, Ra and Nu depend on α, which is only known approximately.

Fig. 8 compares the mean temperature rise of the heater, for the experiments E1 and E2 and for the simulation S2. After a quasi-parabolic evolution, associated with the conductive regime, one observes that the convective regime takes place. It manifests itself by a slower and slightly oscillating evolution of the temperature.

Fig. 9 shows the evolution of the mean height and width of the cells for the experiments and for the simulation. From these curves one can estimate the moving front velocity of the convective cell system: $u_m = \partial_t l_m$. Linear least-squares fitting ($t \geqslant 8$ mn) yield for the experiments: $u_m(\mathrm{E1}) \approx 0.16$ cm mn^{-1}, $u_m(\mathrm{E2}) \approx 0.18$ cm mn^{-1} and for the calculation a little bit smaller value: $u_m(\mathrm{S2}) \approx 0.15$ cm mn^{-1}.

It is also of interest to consider the values of the Rayleigh numbers, say Ra_T and Ra_S, introduced in [14] and found to be important in [31], which are based on the overheating and on the lengthscale $\delta = \sqrt{\kappa_T t_{cr}}$, where t_{cr} corresponds to the onset of the instability phenomenon. For the simulation S2, at $t = t_{cr} \approx t_l = 8$ mn, one obtains $\delta \approx 8.256$ mm, $Ra_T \approx 8570$ and $Ra_S \approx 3110$. One can then check that the so-obtained points (Ra_S, Ra_T) fit well with the experimental diagram produced in [14]. The reasonable idea that imposing a flux density or an exponential-type increase of the heating wall temperature (with a time-constant in the range (75 s, 8000 s)) yields similar results is thus strengthened. Moreover, we obtain $Ra_T/Ra_S^{3/4} \approx 20.6$. Such a value falls in the range 16.3 ± 5, deduced from 36 experiments in [14].

However, the present results only agree qualitatively with those of [37]. When using, as suggested in [37], the characteristic length L^* which makes the Rayleigh

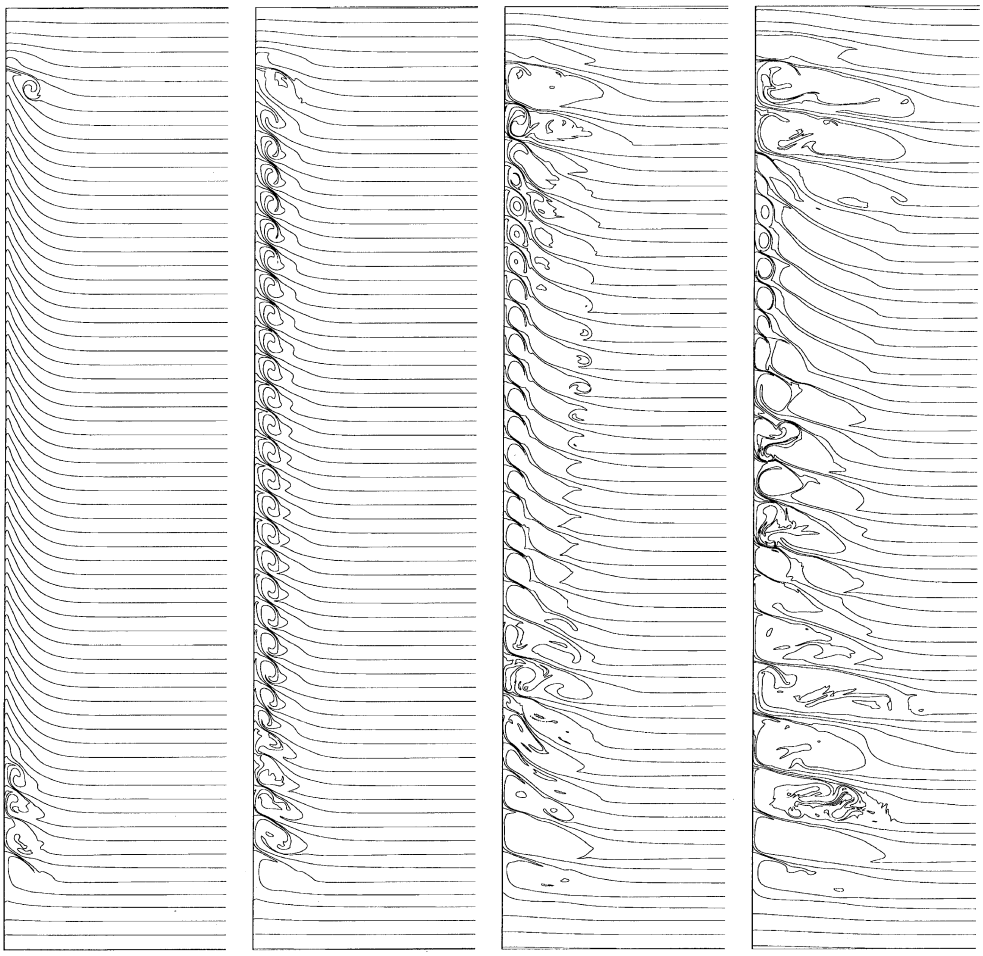

Fig. 5. Salinity S at $t = t_i,\ i = 1,\ldots,4$, for $0 \leqslant x \leqslant 0.68$ and $0.75 \leqslant y \leqslant 3.5$.

number in Eq. (5) equal to 1, we obtain approximately $h_m/L^* \approx 12.5$ and the Reynolds number $Re = h_m u_m/v \approx 0.3$ for our present value of the Nusselt number $Nu \approx 2.50$, rather than values around 24 and 0.8, respectively in [37]. Explanations may be found again due to a poor knowledge of the exact value of the thermal expansion coefficient α, which appears both in Nu and L^*, and, possibly, of an influence of the walls of the rather small tank used in [37], since the choice of L^* as reference length implicitly assumes no influence of the tank walls.

4. Influence of initial disturbances

In this section, we focus on the counter-rotative cells occurrence phenomenon and on the double diffusive instability, in relation to not using (simulation S1) or using (simulation S2) a disturbance of the temperature field at the initial time.

4.1. Counter-rotative cells

Counter-rotative cells are difficult to observe in experiments. Thus, they have not been discerned in the experiments E1 and E2. On the contrary, the linear stability analyses predict the occurrence of alternate co- and counter-rotative cells at the beginning of the convective regime. However, weakly non-linear stability analyses show that bifurcation at the point of marginal stability is subcritical, for both the slot [10] and wide tank [38] cases, so that counter-rotative cells may not be observed. This is why it was interesting to analyze carefully the numerical results, in order to look for an evidence of the existence or non-existence of counter-rotative cells. Fig. 10(a)–(f), obtained

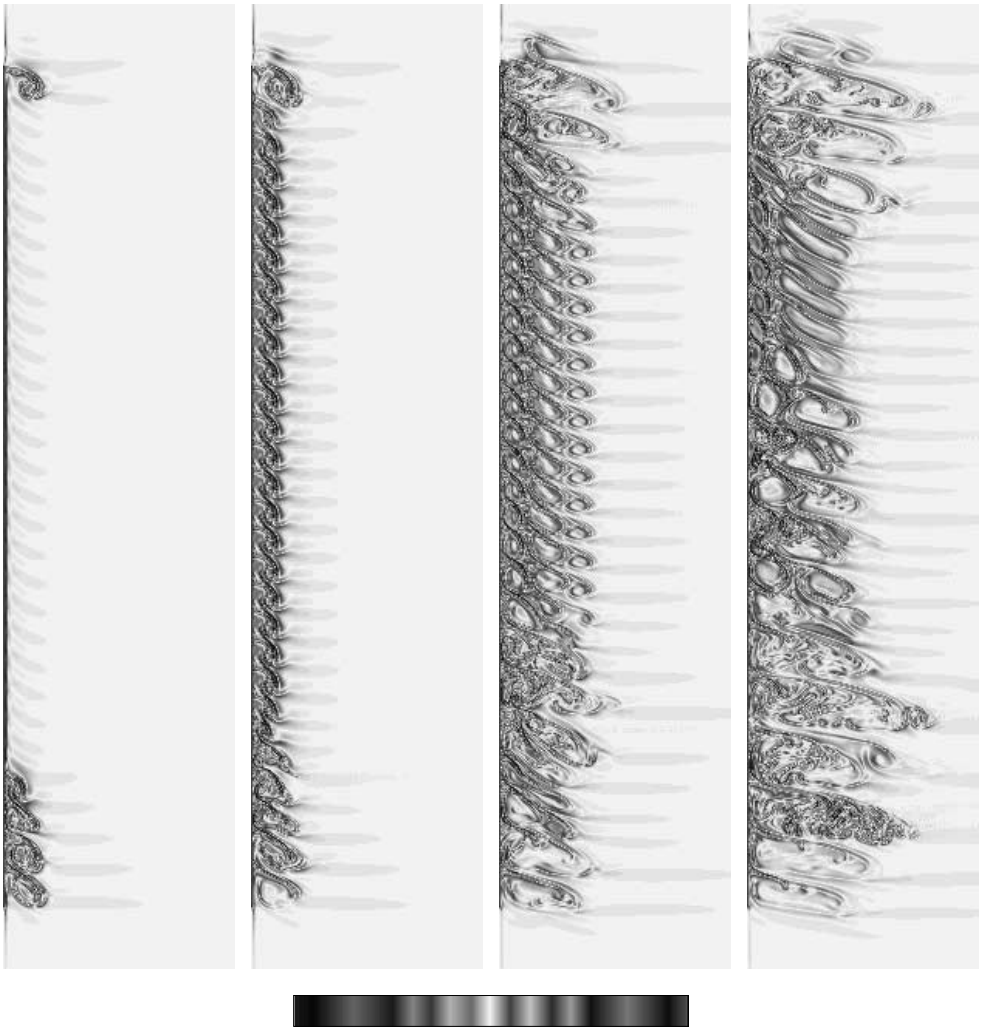

Fig. 6. $\partial_x \rho$, at $t = t_i,\ i = 1, \ldots, 4$, for $0 \leqslant x \leqslant 0.68$ and $0.75 \leqslant y \leqslant 3.5$.

for the simulation S1, goes into the details of the formation of the convective pattern. Successively, (a) the streamlines get distorted, (b) co-rotative cells form, (c) counter-rotative cells appear, (d) amplify and reach their maximum intensity, (e) then weaken till (f) leaving elongated co-rotative cells. Thus, in the present calculation the convective regime does not begin with alternate co- and counter-rotative cells, but counter-rotative cells are clearly observed, for about 35 s.

Another interesting sequence, which is also obtained for the simulation S1, is presented in Fig. 10(g)–(l). This second sequence takes place quickly after the previous one (about 30 s later). Successively, (g) co-rotative cells have gained in intensity, (h) counter-rotative cells form near the heating wall, (i) develop, (j) combine with the co-rotative cells together with new counter-rotative cells formed on the other side, (k) disappear, leaving the latter cells, (l) which finally also disappear, leaving the co-rotative cells of weak intensity. Duration of this second sequence is about 1 mn.

The phenomena described above are much less visible in the simulation S2, are in better agreement with the experiments. Thus, Fig. 11(a)–(d), shows that at the formation of the cell pattern the counter-rotative cells are of weak intensity and remain squeezed between the co-rotative cells. Fig. 11(e)–(h), to be compared to Fig. 10(g)–(l), does not show counter-rotative cells but only points out to a very weak counter-rotative motion near the heating wall.

Counter-rotative cells may also appear when co-rotative cells are merging, as visualized in Fig. 12,

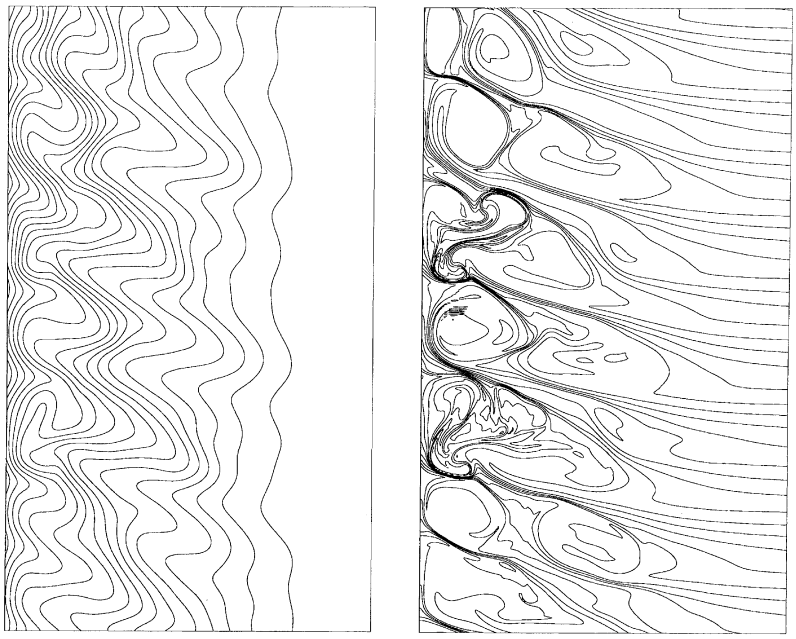

Fig. 7. Details of the temperature and salinity fields at $t = t_F$, $0 \leqslant x \leqslant 0.5$ and $1.75 \leqslant y \leqslant 2.5$.

Table 3
Mean values of the temperature rise of the heater δT_m, of the cell width l_m and of the cell height h_m, ratio K_a and Rayleigh number Ra for the simulation S2

t (min)	δT_m (C)	h_m (cm)	l_m (cm)	K_a	Ra
4	0.78	×	1.03	×	50 402
8	1.07	×	1.49	×	178 486
12	1.15	1.00	2.29	0.41	238 156
16	1.29	1.07	2.81	0.39	377 076
20	1.39	1.08	3.31	0.37	508 311
24	1.43	1.14	3.89	0.38	569 395
28	1.48	1.33	4.57	0.42	653 306

Table 4
Mean values of the temperature rise of the heater δT_m, of the cell width l_m and of the cell height h_m, ratio K_a and Rayleigh number Ra for the experiment E1

t (min)	δT_m (C)	h_m (cm)	l_m (cm)	K_a	Ra
4	0.79	×	1.00	×	39 468
8	1.06	1.30	1.40	0.61	127 927
12	1.19	1.21	2.00	0.51	203 202
16	1.27	1.23	2.70	0.49	263 606
20	1.40	1.36	3.30	0.49	389 271
24	1.44	1.30	4.00	0.45	435 702
28	1.56	1.37	4.90	0.44	600 120

obtained for the simulation S2. In fact, they are of weak intensity, but different gaps are used for the positive and negative values of the stream-function (ratio equal to 10) in order to go into the details of the merging and to show the structure of the interfaces. This sequence clearly shows a merging process: six co-rotative cells

Table 5
Mean values of the temperature rise of the heater δT_m, of the cell width l_m and of the cell height h_m, ratio K_a and Rayleigh number Ra for the experiment E2

t (min)	δT_m (C)	h_m (cm)	l_m (cm)	K_a	Ra
4	0.85	×	1.00	×	67 848
8	1.03	1.25	1.60	0.57	146 288
12	1.16	1.13	2.30	0.46	235 337
16	1.22	1.29	3.10	0.50	287 938
20	1.22	1.36	3.90	0.52	287 938
24	1.26	1.36	4.60	0.51	327 598
28	1.29	1.36	5.40	0.50	359 930

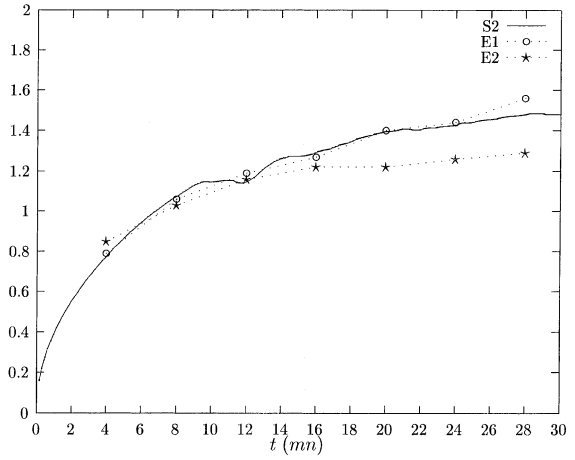

Fig. 8. Mean temperature rise of the heater vs time.

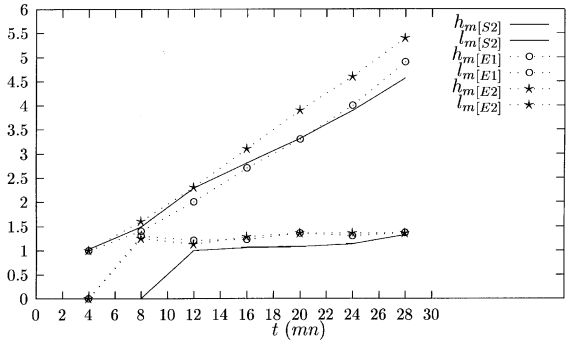

Fig. 9. Mean height and width of the cells vs time.

(Fig. 12(a)) result in four cells (Fig. 12(f)). The merging process is very complex (b)–(e) and induces a weak counter-rotative motion. On the final pattern (f), one can discern the inner cells inside the main ones and very flattened counter-rotative cells at the interfaces of the co-rotative cells of high intensity.

Finally, let us mention that in the simpler situation which assumes periodicity in the vertical direction or when a slot-type domain is considered, the configuration with alternate co- and counter-rotative cells at the beginning of the convective regime is much easier to capture [19,29,39].

4.2. Simultaneous creation of cells

Like for the the simulation S2, or for the experiments E1 and E2, the phenomenon of simultaneous creation of cells is observed for the simulation S1, but it occurs much later than for S2, since the disturbances here only correspond to the approximation and round-off errors. This is visualized in Fig. 13, to be compared with Fig. 3, which shows the stream-function fields at the different times t_i.

Beyond these qualitative comparisons, we have performed a Fourier analysis in y of a nearly periodic part of the flow. Fig. 14 shows the evolution of the most unstable mode of the stream-function for the two simulations and a time-shift is clearly observed. The threshold value, i.e., under which one cannot discern the exponential growth of the Fourier mode, is a pure numerical phenomenon, resulting from the assumption that the extracted part of the flow was perfectly periodic, in order to achieve the Fourier analysis. In the previous calculations [21,27,29], using also a spectral method but for Dirichlet problems, different geometries and different values of the dimensionless parameters, the simultaneous creation was not observed if the initial state was not disturbed: the cavity was filled with cells created successively, before the instability growth was sufficiently high to induce any visible simultaneous creation. On the contrary, one can check again in Fig. 14 that the simultaneous creation process has time to manifest itself before the end of the successive one, for both simulations S1 and S2. Moreover, a linear extrapolation of the straight part of curve (b) till time $t = 0$ yields a value of about 10^{-15}, i.e., comparable to the round-off error. Then, one can guess that for the

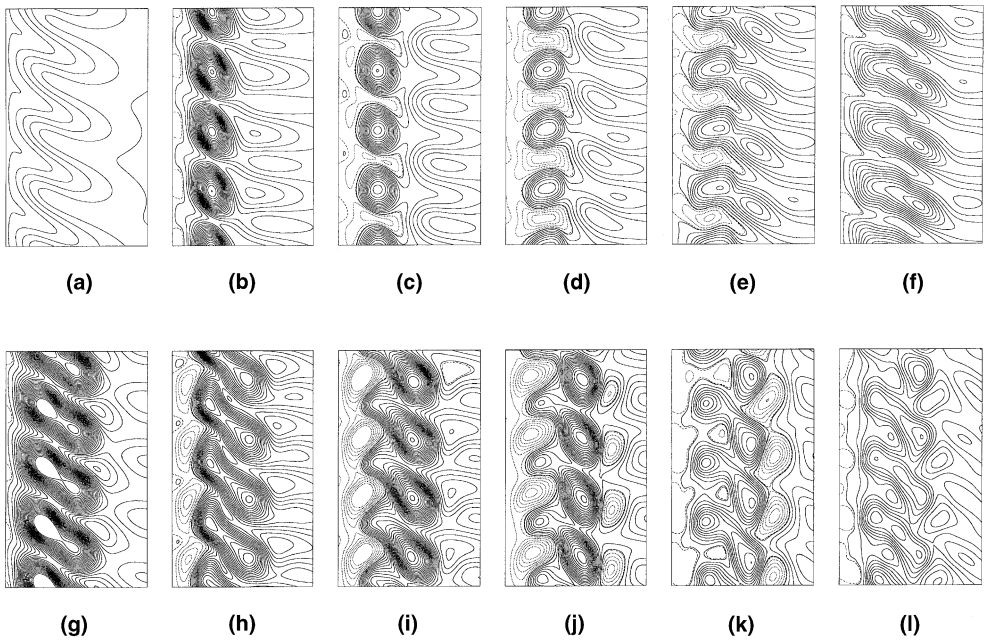

Fig. 10. Details of the flow showing counter-rotative cells for $0 \leqslant x \leqslant 2.4$ cm and $27 \leqslant y \leqslant 31$ cm for the simulation S1, instantaneous streamlines at: (a) $t = 1020$ s, $-1.9420 \leqslant \psi \leqslant 0$; (b) $t = 1070$ s, $-8.1719 \leqslant \psi \leqslant 0.1066$; (c) $t = 1080$ s, $-5.1654 \leqslant \psi \leqslant 0.8300$; (d) $t = 1090$ s, $-2.9600 \leqslant \psi \leqslant 1.6169$; (e) $t = 1100$ s, $-2.8991 \leqslant \psi \leqslant 1.2236$; (f) $t = 1110$ s, $-4.0242 \leqslant \psi \leqslant 0.2070$; (g) $t = 1140$ s, $-9.8070 \leqslant \psi \leqslant 0.0333$; (h) $t = 1160$ s, $-6.3825 \leqslant \psi \leqslant 1.4993$; (i) $t = 1170$ s, $-8.0776 \leqslant \psi \leqslant 3.1357$; (j) $t = 1180$ s, $-6.2141 \leqslant \psi \leqslant 2.3842$; (k) $t = 1190$ s, $-3.1768 \leqslant \psi \leqslant 1.9291$; (l) $t = 1200$ s, $-3.5403 \leqslant \psi \leqslant 0.2063$ (N.B. full lines are used for negative values).

present fluid flow problem, the sole round-off errors would have induced the double diffusive instability, even if the approximation errors were negligible. Consequently, although if it is difficult to discern the influence of the round-off and approximation errors, one may think that it is natural to observe instability in the present calculation, although no artificial disturbances have been superimposed to the initial conditions.

In order to go farther in this analysis of cell creation, it is of interest to consider the flow computed in [22], where it is not a spectral but a less accurate finite volume method which is used. The computational domain is $]0, L[\times]0, H[$ with $H/L = 2$. At the initial time the fluid is at rest, the temperature is homogeneous and the salinity gradient is constant and downwards. For the boundary conditions, (i) temperatures of the vertical walls are imposed and adiabaticity is assumed at the top and bottom of the cavity, (ii) homogeneous Neumann conditions are used everywhere for salinity, and (iii) no-slip conditions are used for velocity. The characteristic parameters of the fluid are $Pr = 7$ and $Le = 100$. The characteristic parameters of the flow are $Ra = 2.33 \times 10^5$ and $R_\rho = 7$. These values are based on the temperature difference between the vertical walls and on the scale h_a.

The spectral calculations have been performed using a very fine grid: $150 \times 120 \times 8$ (i.e., 150×120 grid-points in eight sub-domains). Fig. 15 presents instantaneous streamlines which can be compared to the results presented in Fig. 3 of [22]. We note that the spectral calculation does not show the simultaneous creation of cells, but only a successive one, which means that, as in [21,27,29], due to a lower instability growth rate and different geometrical parameters the approximation and round-off errors are not sufficient here to cause the double diffusive instability. However, it has been checked that the simultaneous creation of cells is obtained with a slight disturbance of the initial temperature field. Adding a 10^{-4} random perturbation to this field induces the double diffusive instability, once the first convective cells in the lower and upper parts are created. Thus, the high accuracy of the present calculation prevents us to obtain what seemed to be observed in [22]. However, reminding that the simulation S2 had to be preferred to the simulation S1 for the sake of comparison with laboratory experiments, one can also assume that the calculation of [22] would be in better agreement with the experimental data. Thus we recover here that numerical approximations generally work as the unavoidable experimental disturbances and even that it is natural to add some disturbances at the

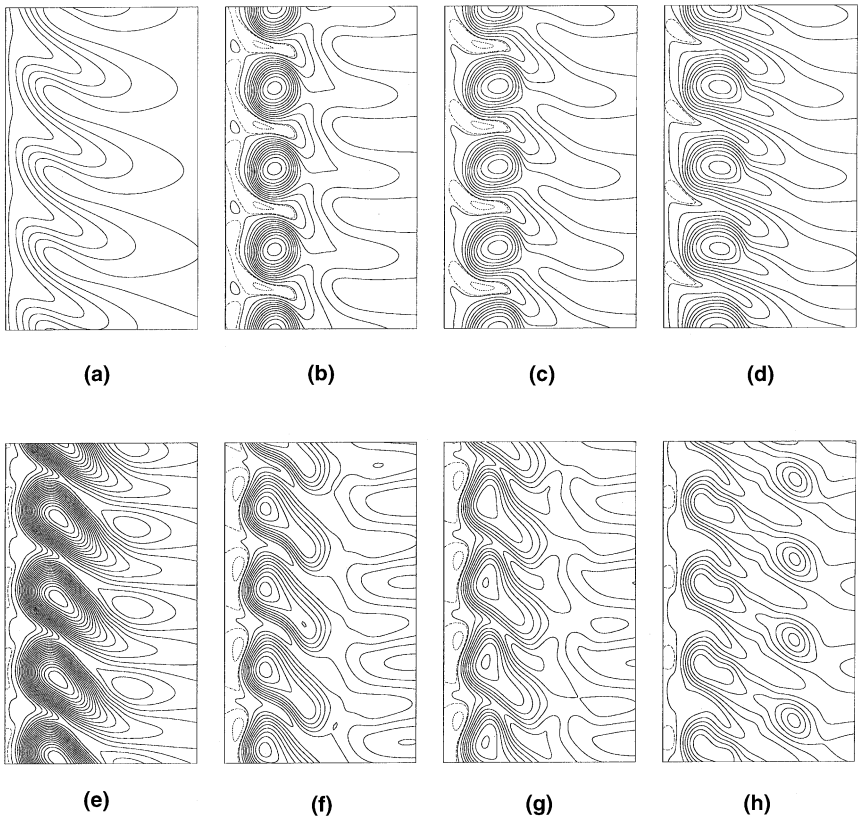

Fig. 11. Details of the flow showing counter-rotative cells for $0 \leqslant x \leqslant 2.4$ cm and $27 \leqslant y \leqslant 31$ cm for the simulation S2, instantaneous streamlines at: (a) $t = 550$ s, $-2.0483 \leqslant \psi \leqslant 0$; (b) $t = 610$ s, $-4.0283 \leqslant \psi \leqslant 0.3336$; (c) $t = 620$ s, $-3.3678 \leqslant \psi \leqslant 0.3587$; (d) $t = 630$ s, $-3.3337 \leqslant \psi \leqslant 0.1108$; (e) $t = 680$ s, $-7.5870 \leqslant \psi \leqslant 0.0101$; (f) $t = 720$ s, $-3.7137 \leqslant \psi \leqslant 0.4443$; (g) $t = 730$ s, $-3.2368 \leqslant \psi \leqslant 0.3933$; (h) $t = 760$ s, $-3.0132 \leqslant \psi \leqslant 0.0342$ (N.B. full lines are used for negative values).

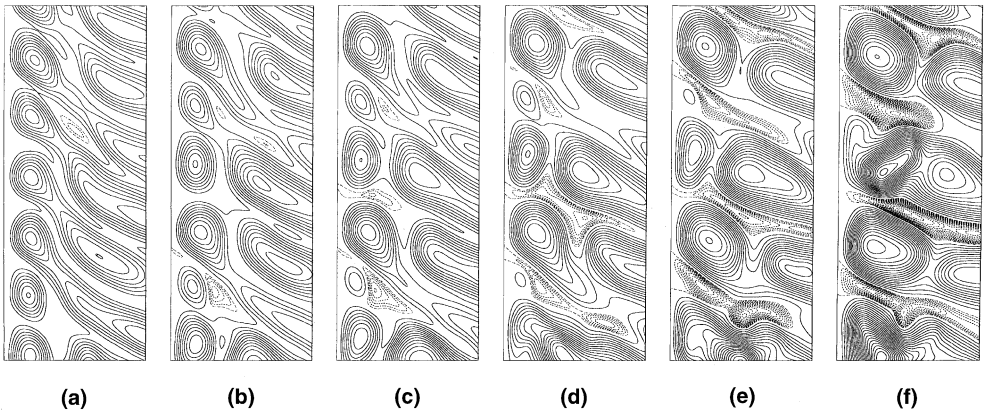

Fig. 12. Details of the flow showing merging of cells for $0 \leqslant x \leqslant 2.4$ cm and $27 \leqslant y \leqslant 31$ cm for the simulation S2, instantaneous streamlines at: (a) $t = 1400$ s, $-5.1758 \leqslant \psi \leqslant 0.1512$; (b) $t = 1540$ s, $-5.9224 \leqslant \psi \leqslant 0.3719$; (c) $t = 1600$ s, $-7.2252 \leqslant \psi \leqslant 0.5355$; (d) $t = 1660$ s, $-8.2289 \leqslant \psi \leqslant 0.6457$; (e) $t = 1720$ s, $-11.543 \leqslant \psi \leqslant 1.3000$; (f) $t = 1780$ s, $-12.935 \leqslant \psi \leqslant 1.7220$ (N.B. full lines are used for negative values).

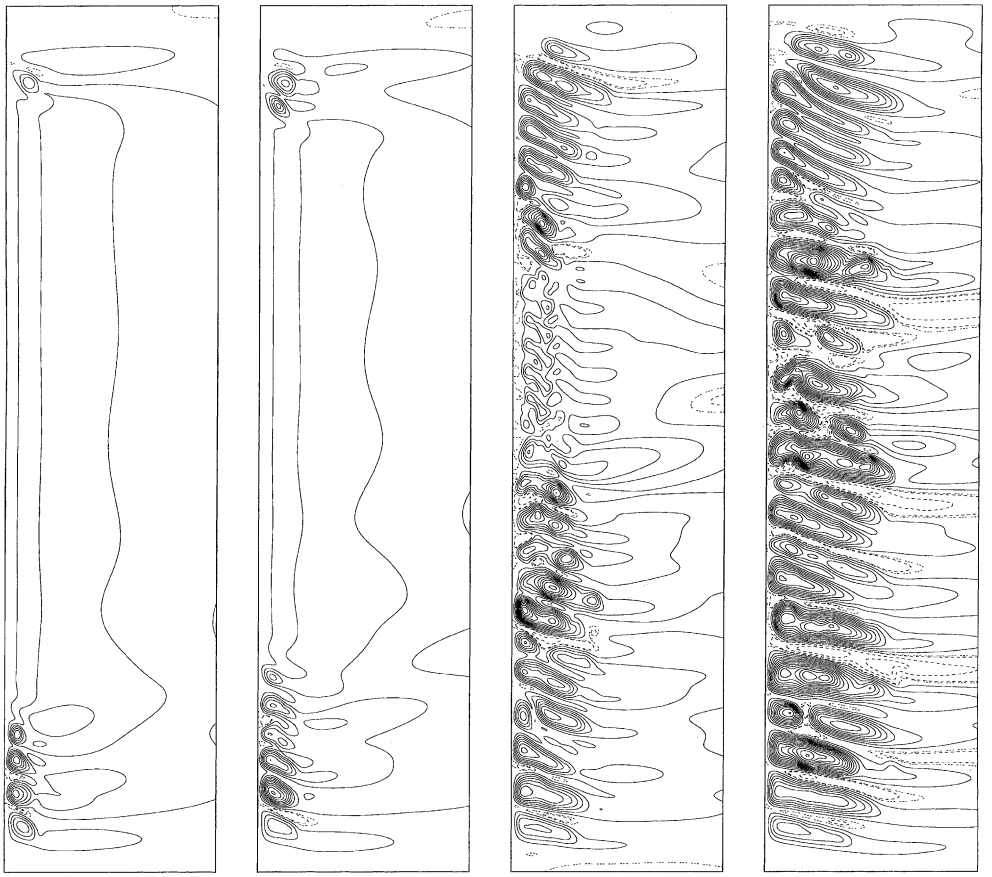

Fig. 13. Stream-function ψ at $t = t_i,\ i = 1, \ldots, 4$, for $0 \leqslant x \leqslant 0.68$ and $0.75 \leqslant y \leqslant 3.5$, simulation S1 (N.B. full lines are used for negative values).

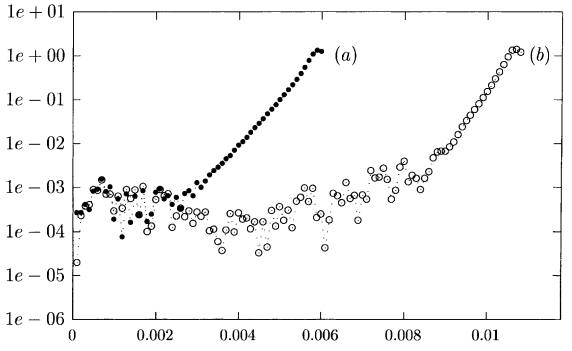

Fig. 14. Stream-function most instable Fourier mode vs time, at $x = 0.045$ and for $2.25 \leqslant y \leqslant 2.58$: with (a) and without (b) initial random disturbance on T.

initial time, as done in the theoretical analyses of stability, when a highly accurate numerical method is used.

5. Conclusion

Thanks to the use of a well-adapted multi-domain Chebyshev spectral method, a reliable calculation of a complex double diffusive convective flow has been carried out. As a result, the experimental and numerical evolutions of the flow patterns and of characteristic quantities agree rather well. The numerical approach has permitted a detailed study of the cell formation process. Especially we have focused on the possible existence of counter-rotative cells and on the phenomenon of simultaneous creation of convective cells, before the end of the successive one. It has appeared that both the phenomena, existence of counter-rotative cells and simultaneous creation of cells, are very sensitive to weak disturbances of the initial state: counter-rotative cells are of stronger intensity and the delay required to observe the double diffusive instability is much greater when the initial state is not disturbed. Such a numerical evidence may give answers to those not clearly understood

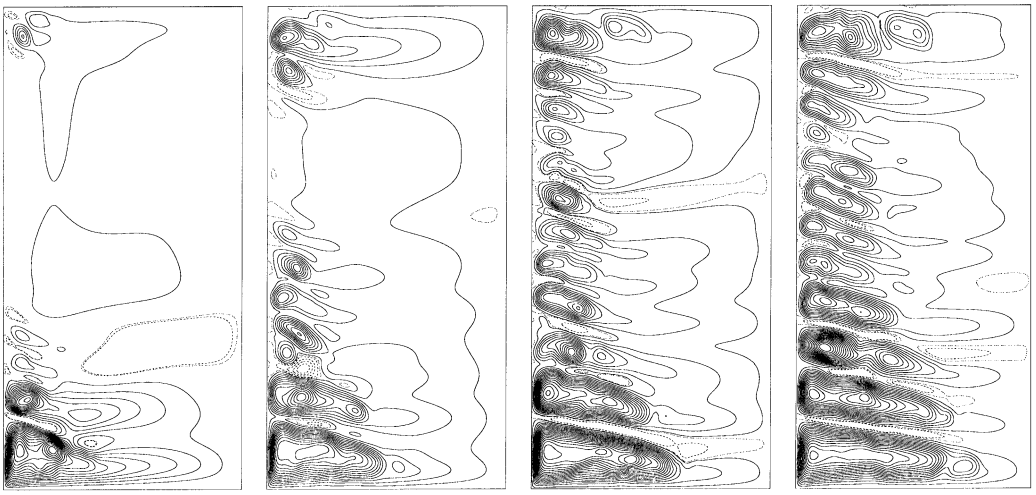

Fig. 15. Instantaneous streamlines at $t = \{0.005, 0.01, 0.015, 0.02\}$ (N.B. full lines are used for negative values).

distortions between the experimental studies and numerical, or theoretical, investigations.

Acknowledgements

This study was done in the framework of a cooperation supported by the CNRS, the Russian Academy of Sciences and the University of Nice-Sophia Antipolis. The calculations have been done on the CRAY T3E supercomputer of the IDRIS French centre. We also thank J.M. Lacroix for his helpful technical support.

References

[1] K.N. Fedorov, The Thermohaline Fine Structure of the Ocean, Pergamon Press, New York, 1978.
[2] J.S. Turner, Double diffusive phenomena, Ann. Rev. Fluid Mech. 6 (1974) 37–56.
[3] J.S. Turner, Multicomponent convection, Ann. Rev. Fluid Mech. 17 (1985) 11–44.
[4] P.F. Linden, J.E. Weber, The formation of layers in a double diffusive system with a sloping boundary, J. Fluid Mech. 81 (1977) 757–773.
[5] V.A. Popov, Yu.D. Chashechkin, Free convection around a horizontal cylinder in a stratified liquid, Soviet Phys. – Tech. Phys. 25 (1980) 1276–1282.
[6] Yu.D. Chashechkin, V.S. Tupitsyn, Structure of free convective flow over a point source of heat in a stratified liquid, Soviet Phys. – Doklady 24 (1979) 862–864.
[7] A.B. Tsinober, Y. Yahhalom, D.J. Shlien, A point source of heat in a stable salinity gradient, J. Fluid Mech. 135 (1983) 199–217.
[8] P.K. Thorpe, S.A. Hutt, R. Soulsby, The effect of horizontal gradients on thermohaline convection, J. Fluid Mech. 38 (1969) 375–400.
[9] J.E. Hart, On sideways diffusive instability, J. Fluid Mech. 49 (1971) 279–288.
[10] J.E. Hart, Finite amplitude sideways diffusive convection, J. Fluid Mech. 59 (1973) 47–64.
[11] R.A. Wirtz, C.S. Reddy, Experiments on convective layer formation and merging in a differentially heated slot, J. Fluid Mech. 91 (1979) 451–464.
[12] C.F. Chen, D.G. Briggs, R.A. Wirtz, Stability of thermal convection in a salinity gradient due to lateral heating, Int. J. Heat Mass Transfer 14 (1971) 57–66.
[13] V.N. Nekrasov, V.A. Popov, Yu.D. Chashechkin, Formation of periodic convective-flow structure on lateral heating of a stratified liquid, Izv. Atmos. Ocean. Phys. 12 (1976) 1191–1200.
[14] A.B. Tsinober, J. Tanny, On the structure and dynamics of double diffusive layers in sidewall heating experiments, in: N.E. Bixler, E. Spiegel (Eds.), Proceedings of the ASCE/ASME Mechanics Conference on Double Diffusive Motions, ASME, 1985, pp. 39–45.
[15] J. Tanny, A.B. Tsinober, The dynamics and structure of double-diffusive layers in sidewall-heating experiments, J. Fluid Mech. 196 (1988) 135–156.
[16] C.G. Jeevaraj, J. Imberger, Experimental study of double-diffusive instability in sidewall heating, J. Fluid Mech. 222 (1991) 565–586.
[17] V.V. Levitskii, Yu.D. Chashechkin, Thermoconcentration-related convection at the inclined wall, Phys. – Doklady 41 (1996) 615–618.
[18] T. Nishimura, O. Yasuyuki, S. Sakura, A.M. Morega, Interfacial breakdown of double-diffusive convective layers by a horizontal temperature gradient, Int. J. Heat Mass Transfer 42 (1999) 1479–1489.
[19] R.A. Wirtz, L.H. Liu, Numerical experiments on the onset of layered convection in a narrow slot containing a stably stratified fluid, Int. J. Heat Mass Transfer 18 (1975) 1299–1305.
[20] J.C. Heinrich, A finite element method for double diffusive convection, Int. J. Numer. Methods Eng. 20 (1984) 465–477.

[21] Y. Demay, J.M. Lacroix, R. Peyret, J.M. Vanel, Numerical experiments on stratified fluids subject to heating, in: E.J. List, G.H. Jirka (Eds.), Proceedings of the Third International Symposium on Stratified Flows, Pasadena, 1987, American Society of Civil Engineers, New York, 1990, pp. 588–597.
[22] J.W. Lee, J.M. Hyun, Double-diffusive convection in a cavity under a vertical solutal gradient and a horizontal temperature gradient, Int. J. Heat Mass Transfer 34 (1991) 2423–2447.
[23] J. Wright, W. Shyy, Numerical simulation of unsteady convective intrusions in a thermohaline stratification, Int. J. Heat Mass Transfer 39 (1996) 1183–1201.
[24] S.G. Schladow, E. Thomas, J.R. Koseff, The dynamics of intrusions into a thermohaline stratification, J. Fluid Mech. 236 (1992) 127–165.
[25] H.A. Dijkstra, E.J. Kranenborg, On the evolution of double-diffusive into a stably stratified liquid: the physics of self-propagation, Int. J. Heat Mass Transfer 41 (1998) 2113–3124.
[26] E.J. Kranenborg, H.A. Dijkstra, On the evolution of double-diffusive into a stably stratified liquid: a study of the layer merging process, Int. J. Heat Mass Transfer 41 (1998) 2743–2756.
[27] R. Peyret, J.M. Vanel, Numerical experiments in double-diffusive convection, in: D. Leutloff, R.C. Srivastava (Eds.), Computational Fluid Dynamics, Springer, Berlin, 1995, pp. 33–52.
[28] C. Sabbah, R. Pasquetti, A divergence-free multi-domain spectral solver of the Navier–Stokes equations in geometries of high aspect ratio, J. Comput. Phys. 139 (1998) 359–379.
[29] C. Sabbah, Etude par méthode spectrale multi-domaine et calcul parallèle d'écoulements de convection thermosolutale en cavité chauffée latéralement, Thesis of the University of Nice-Sophia Antipolis, 2000.
[30] C.F. Chen, F. Chen, Salt-finger convection generated by lateral heating on a solute gradient, J. Fluid Mech. 352 (1997) 161–176.
[31] O. Kerr, Heating a salinity gradient from a vertical sidewall: linear theory, J. Fluid Mech. 207 (1989) 323–352.
[32] V.V. Levitskii, Yu.D. Chashechkin, Thermoconcentration convection under uniform lateral heating, Fluid Dynamics 30 (1995) 718–724.
[33] C. Canuto, M.Y. Hussaini, A. Quarteroni, T.A. Zang, Spectral Methods in Fluid Dynamics, Springer, Berlin, 1988.
[34] J.S. Turner, Double diffusive intrusions into a density gradient, J. Geophys. Res. 83 (1978) 2887–2901.
[35] A.V. Kistovich, Yu.D. Chashechkin, Generation of dissipative gravity waves during free convection in a stratified medium, J. Appl. Mech. Tech. Phys. 32 (1991) 342–348.
[36] Y. Suzukawa, U. Narusawa, Structure of growing double diffusive convection cells, J. Heat Transfer 104 (1982) 248–254.
[37] U. Narusawa, Y. Suzukawa, Experimental study of double-diffusive cellular convection due to a uniform lateral heat flux, J. Fluid Mech. 113 (1981) 387–405.
[38] O. Kerr, Heating a salinity gradient from a vertical sidewall: nonlinear theory, J. Fluid Mech. 217 (1990) 529–546.
[39] C.S. Reddy, Cell merging and its effects on heat transfer in thermo-solutal convection, J. Heat Transfer 102 (1980) 172–174.